Acta Crystallographica Section A
Foundations of Crystallography
ISSN 0108-7673

Received 31 January 2005
Accepted 9 May 2005

Improved data acquisition in grazing-incidence X-ray scattering experiments using a pixel detector

C. M. Schlepütz, R. Herger, P. R. Willmott,* B. D. Patterson, O. Bunk, Ch. Brönnimann, B. Henrich, G. Hülsen and E. F. Eikenberry

Swiss Light Source, Paul Scherrer Institute, CH-5232 Villigen, Switzerland. Correspondence e-mail: philip.willmott@psi.ch

The use of an area detector in grazing-incidence X-ray experiments lends many advantages in terms of both speed and reliability. Here a discussion is given of the procedures established using the PILATUS pixel detector developed at the Swiss Light Source for optimizing data acquisition and analysis of surface diffraction data at the Materials Science beamline, especially with regard to reflectivity measurements, crystal truncation and fractional order rods, and grazing-incidence diffraction experiments.

1. Introduction

Experimental problems in grazing-incidence small-angle X-ray scattering and surface X-ray diffraction studies (GISAXS and SXRD, respectively) are characterized by several features (Feidenhans'l, 1989; Robinson, 1991; Robinson & Tweet, 1992). These include the following.

- A low scattered/diffracted signal intensity, depending on the systems studied; although strongly scattering transition-metal and complex metal oxide surfaces certainly provide sufficient count rates, self-assembled organic monolayers and even silicon have a scattering power so low that third-generation synchrotron sources are definitely mandatory.
- A need to determine precisely the intensity correction factors as a function of the sample and detector angles and slit settings.
- The danger that unidentified signals originating from some unforeseen source (*e.g.* diffuse scattering signal, Yoneda peaks or part of the sample mounting equipment) can be misinterpreted as part of the signal under investigation. Much of this can in principle be minimized by restrictive slit settings but in practice many samples are small and cannot be mounted without having some part of the mounting mechanism in the incident beam. We discuss this in more detail with regard to our 'open slit' configuration below.
- Difficulties in maintaining a clean and well defined sample over extended periods of time, a particular problem in surface diffraction studies.

By using a single-photon counting area detector with fast read-out times, all of the above problems can be handled with relative ease. The speed of acquisition and the lack of electronic noise makes this detector technology superior to conventional charged-coupled-device (CCD) arrays (Alvarez *et al.*, 2000; Jensen *et al.*, 2002; Tancret *et al.*, 2004), especially for surface diffraction experiments, in which weak signal intensity is often measured.

In this article, we describe how the features of an in-house-built pixel detector have enabled us to record grazing-incidence X-ray diffraction data with unprecedented accuracy and speed at the surface diffraction station of the Materials Science (MS) beamline at the Swiss Light Source (Patterson *et al.*, 2005). The data correction factors required for operating in this mode are presented as they are different from those used when recording with a point detector. The most important differences are the following.

- We use neither entrance nor exit slits, *i.e.* the unrestricted beam is allowed to flood the sample and the entire diffraction reflection is acquired, independent of the detector angles. This is unusual, as, in classical SXRD, the sampled surface is given by a parallelogram defined by entrance slits restricting the extent of the incident beam in the plane of the sample, and exit slits defining the part of the irradiated stripe on the surface seen by the detector. For a fixed set of entrance and exit slits, this sets a lower limit to the detector angle below which the parallelogram extends beyond the physical size of the sample.
- No sample rotation scan is required to record each point (*i.e.* l value) along the crystal truncation and fractional order rods (CTRs and FORs, respectively) as the full extent of the CTR signal where it intersects the Ewald sphere is recorded in a single image. This is similar to the stationary mode described by Specht & Walker (1993) and Vlieg (1997), and recently validated by Torrelles & Rius (2004), with the added advantages that the entire signal can be integrated, thereby improving the statistics, and the fact that there is no danger of gradually drifting off the 'maximum intensity ridge' as one moves along l.

2. Crystal truncation rods

Rigorous descriptions of crystal truncation rods and surface diffraction can be found elsewhere (Feidenhans'l, 1989; Robinson & Tweet, 1992; Als-Nielsen & McMorrow, 2001). Here, only the quintessential features are briefly described in order to understand the remainder of the text. CTRs provide detailed information on the surface structures of crystalline materials and how they differ from those of the bulk. They result from a smearing out of an ideal diffraction pattern by its convolution with the $1/k_z$ shape function of an atomically flat surface, whereby k_z is the reciprocal-space coordinate perpendicular to the surface normal.

Even for samples with atomically flat surfaces, the signal intensity along a CTR as one moves away from Bragg peaks rapidly weakens as scattering from the different atomic layers becomes increasingly destructive. For an unreconstructed surface, the intensity exactly in between Bragg peaks is of the same order of magnitude as that from a single atomic layer. This is the reason why surface diffraction is only practical using the intense flux of synchrotron radiation and why low background noise is essential.

How does one record a CTR? The specular, or (00*l*), rod is recorded like a reflectivity curve. All other rods are non-specular, *i.e.* recorded using a constant grazing-incidence angle, and require a concerted movement of at least three motor movements (in our case, ω, δ and γ, see Fig. 1). A schematic of the movements of the (2 + 3) surface diffractometer used at the Swiss Light Source and the relationship between the pertinent vectors in reciprocal space when recording a nonspecular CTR scan are given in Fig. 2 (Vlieg, 1998; You, 1999).

3. The 'PILATUS' area pixel detector

The PILATUS detector was developed for protein crystallography. It consists of an array of 3×6 silicon modules, covering an area of 21×24 cm^2. Details of the detector can be found in Brönnimann *et al.* (2003). Briefly, it is a fast digital X-ray camera operated in single-photon counting mode. The main features include: no dark current background; no readout noise; an excellent point spread function; and short readout time. The detector used here is a single PILATUS module with adapted readout electronics and software. It consists of an array $\mathcal{A}$ of 366×157 pixels, each with dimensions 217×217 µm^2, covering an active area of 7.9×3.4 cm^2.

A major advantage of the pixel detector is the pulse-height threshold, which can be set individually in each pixel, and which eliminates any dark noise. This threshold setting has an intrinsic energy resolution of approximately 1 keV. Prior to exposure with X-rays, an internal calibration circuit is used to adjust the lower threshold in each pixel to a predefined value. This so-called threshold trimming is described in Eikenberry *et al.* (2003). The thickness of the silicon sensor is 300 µm. The corresponding X-ray absorption is >95% below 8 keV, 74% at 12 keV and 25% at 20 keV, hence the absorption properties are well matched to the available energy range of the MS beamline (Patterson *et al.*, 2005).

The effective angle subtended by each pixel depends on the distance between the pixel detector and the sample (presently 1.235 m), the sample size, and the size and position of any apertures between them. In the present configuration at the MS beamline, and assuming an infinitely small sample size, each pixel subtends an angle of 0.0101°, hence the whole detector subtends a solid angle of $3.70° \times 1.59°$. In practice, each pixel sees the whole irradiated part of the sample, since large detector entrance slits are used (see below). The resolution of any given pixel is therefore given by the range of exit angles of beams scattered from different parts of the irradiated sample surface.

Using this geometry, the size of the area detector was found to be ideal – a large detector area is convenient, since signals are more easily found, and, at low exit angles, where the CTRs puncture the Ewald sphere close to its base (see Fig. 2), nearly the whole length of the detector may be illuminated by the extended signal. This is especially noticeable for the generally more diffuse superstructure FORs, which may extend significantly in the surface *h* and *k* directions and therefore intersect a larger portion of the Ewald sphere. The detector has a sufficiently high resolution, even for perfect crystals such as Si, to always have at least of the order of ten or more pixels inside a peak.

A detector flight tube with a rectangular profile mounted on the front of the pixel detector extends as far as possible towards the sample at the centre of the diffractometer, and is in the present set-up 0.80 m long. It is flushed with helium and suppresses stray signals due to air scattering and diffraction cones originating from the direct beam passing through container walls (*e.g.* beryllium windows *etc.*). At present, the maximum number of counts recorded by each pixel in any given image should be kept around or below 10000. The short

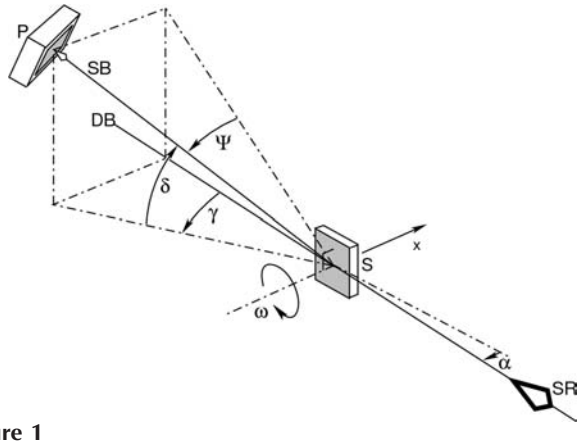

Figure 1
Relevant angles and motor movements of the (2 + 3)-circle diffractometer used at the surface diffraction station of the Materials Science beamline, SLS. Sample circles: α and ω. Detector circles: δ, γ and ν (detector rotation not shown). Ψ is defined as a function of δ and γ in the text and is the angle between the scattered beam and the sample surface. *x*: linear translation of sample parallel to the ω axis. Positive directions are indicated by the arrow heads. SR = synchrotron radiation, S = sample, DB = direct beam, SB = scattered beam, P = pixel area detector.

readout time allows a maximum data acquisition rate of 30 images s^{-1}.

4. Image correction

4.1. Flat-field signal source

The module was one of the earliest of a small volume production. It suffers from very inhomogeneous charge collection over the pixel array, *i.e.* the sensitivity of each pixel element in the detector differs significantly. This efficiency is not related to the threshold value of each pixel. Instead, it is basically defined by the effective sensitive volume of each pixel, from which the charge generated by absorption of the X-rays is detected. In more recent modules, the sensitive volume per pixel is far more uniform throughout the detector.

The recorded images are corrected for this variation in sensitivity by a normalization mask array, created by recording images of a spatially homogeneous ('flat-field') signal. This is typically performed by inserting a sample into the direct beam that contains an element with a strong fluorescence signal at an energy above the lower threshold of the detector but with the corresponding absorption edge below the synchrotron photon energy. So, for example, with synchrotron radiation at 12.398 keV (1 Å) and a lower threshold of 8 keV for the detector, we used a sliver of single-crystal GaAs.[1] Ga and As have K 1s electron binding energies of 10.367 and 11.867 keV, respectively, and strong K fluorescent lines between 9.225 and 11.86 keV.

4.2. Aberrant pixels

The procedure for flat-field correction typically involves recording several tens of images. This not only improves the statistics of the flat-field normalization mask but also serves a second purpose. A small fraction of the pixels produces anomalous signals, which must be identified and corrected. A histogram of the frequency of pixel counts is generated for a typical flat-field image, as shown in Fig. 3. The main broad feature is the true flat-field signal. The upper and lower limits of this region are estimated and all signal lying outside this is judged as being anomalous. This consists of a single peak at zero counts, associated with dead pixels (discussed in detail below), and grasslike signal either side of the main feature, representing the small fraction of spurious pixels.

The reliability of each of the 57 462 pixels is then assessed in the following manner: For each of the m flat-field images, it is checked whether pixel (i, j) $(0 \leq i \leq 365,\ 0 \leq j \leq 156)$ has a count I that lies within or outside the 'normal' region of the histogram. If a pixel lies outside this region more than a certain fraction x of the time, it is deemed to be anomalous. The coordinate (i, j) of that pixel is then flagged in a second 'binary' mask array $\mathcal{B}$ of the same size as the pixel array and set from unity to zero. For those pixels that produce an anomalous signal less than $m(1 - x)$ times, the median value is taken of the normal count events and used for the flat-field mask. The final flat-field mask $\mathcal{F}$ is generated by taking the reciprocal of each averaged count, normalizing the array to unity and multiplying by the binary mask $\mathcal{B}$, *i.e.*

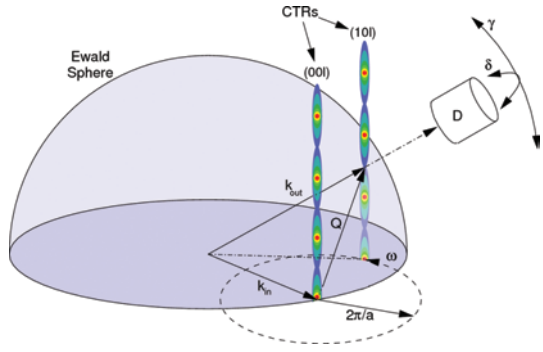

Figure 2
A schematic diagram of how one records non-specular CTRs, shown in reciprocal space for the example of the (10l) CTR. Here we show the specular (00l) and the (10l) rods only, for the sake of clarity. They are separated from one another in reciprocal space by $2\pi/a$, where a is the lattice constant in the plane. The incoming X-ray beam (k_{in}) is at grazing incidence ($\alpha \approx 0^{\circ}$). As the sample rotates about its normal (ω), so do the nonspecular CTRs around the specular rod by the same amount. The X-rays are elastically scattered by an amount Q. The scattered diffraction signal is found in the direction of the vector k_{out}, defined by the origin of the Ewald sphere and the point where the (10l) rod penetrates the Ewald sphere. In order to track this signal with the detector D, the δ and γ motors of the detector arm and the sample rotation ω must move in a concerted manner as a function of l.

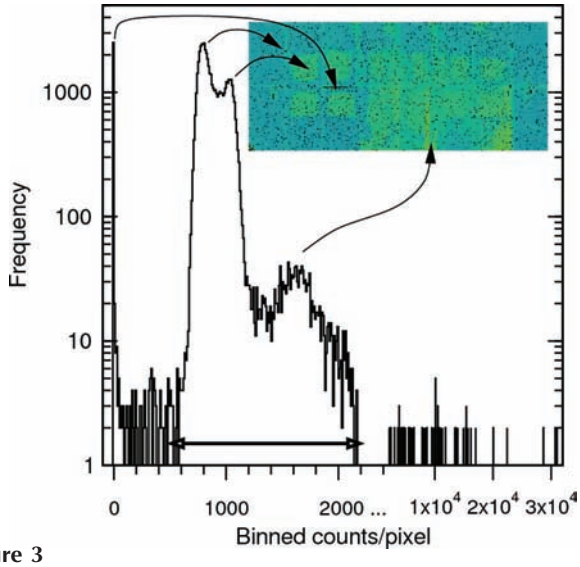

Figure 3
A histogram of a typical flat-field image. Here, the counts/pixel have been collected into bins of width 10 counts, in order to simplify the analysis. Certain regions of the detector have a reduced charge-collection efficiency, as is evident in the lighter and darker patches, which result in the double peak in the main feature of the histogram. There are also about 5% of dead pixels, resulting in a sharp peak at the start of the histogram. Pixels associated with signal outside the arrowed region (approximately 500 to 2200 counts) are deemed to be unreliable and removed using the flat-field binary mask.

[1] There is a very small chance that the crystal is so oriented that it satisfies the Bragg condition and that the detector is in the correct position to record a Bragg peak, in which case the crystal must be slightly repositioned.

$$\mathcal{F}(i,j) = \left(\frac{m\overline{I}_{\max}}{\sum_m \mathcal{A}(i,j)}\right)\mathcal{B}(i,j), \quad (1)$$

where $\overline{I}_{\max}$ is the maximum value of the averaged array $\overline{\mathcal{A}(i,j)}$.

Because the array $\mathcal{F}$ contains zeros from the binary mask, raw pixel-detector data images corrected by multiplication with $\mathcal{F}$ will also contain the same pattern of zeros. We have chosen to correct for these by replacing them with the mean value of the counts of the eight nearest-neighbour pixels.

Lastly, any pixel can occasionally be anomalously 'hot', although it passed the criterion described above for the binary mask. These relatively rare events are filtered out using a so-called 'median filter' by recording the same image an odd number of times (*e.g.* 3 or 5) and, for each pixel position, selecting the median value.

The change in the appearance of a typical signal is shown for the different stages of correction and filtering in Fig. 4.

5. Data errors and correction factors

Here, we describe the most important aspects of error sources. Although most of the geometrical correction factors are not new, a full description of them is also given for completeness, particularly in view of the unusual recording mode of open slits and sample flooding.

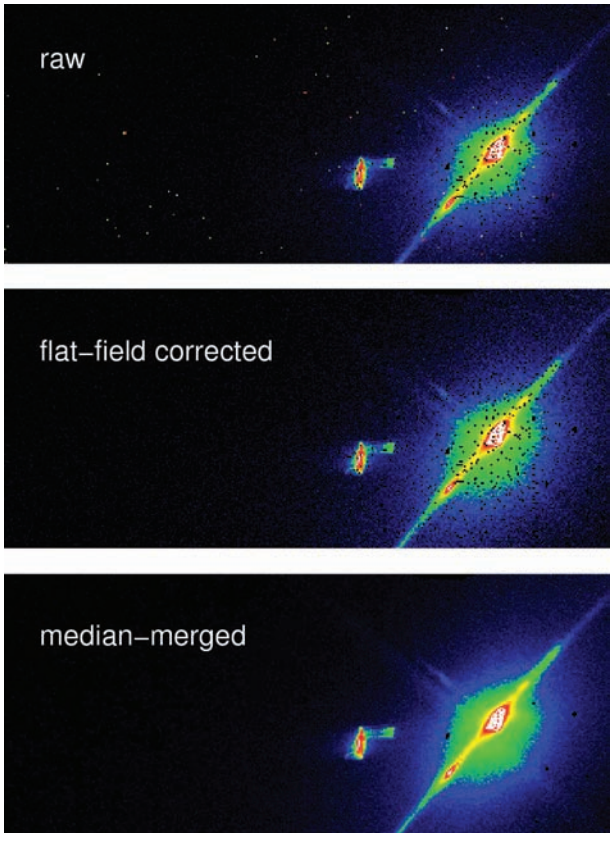

Figure 4
The improvement of the raw image quality after flat-field correction and median merging. The image shows a CTR (small feature to the left) in the neighborhood of a Bragg peak.

5.1. Background subtraction and sources of errors

Once the images have been flat-field corrected and anomalous pixel signals have been removed, data are obtained in the simplest case (*e.g.* as used in 'on-the-fly' analysis, see Fig. 5) by integrating a region that contains the entire signal (S) and subtracting from that a representative integrated background signal B, *i.e.*

$$I = S - B, \quad (2)$$

where the magnitude of B is scaled by A_S/A_B, A_S (A_B) being the number of pixels integrated in obtaining S (B).

Although this simple 'box subtraction' is satisfactory for rapid analysis during data acquisition, a more sophisticated background subtraction method could be applied, using contour mapping, for the final analysis.

The statistical errors associated with the structure factor F, proportional to $I^{1/2}$, are in general less than a percent, except for points far from Bragg peaks and surfaces with low scattering power. The main sources of error are systematic in nature. They may arise from several factors, of which

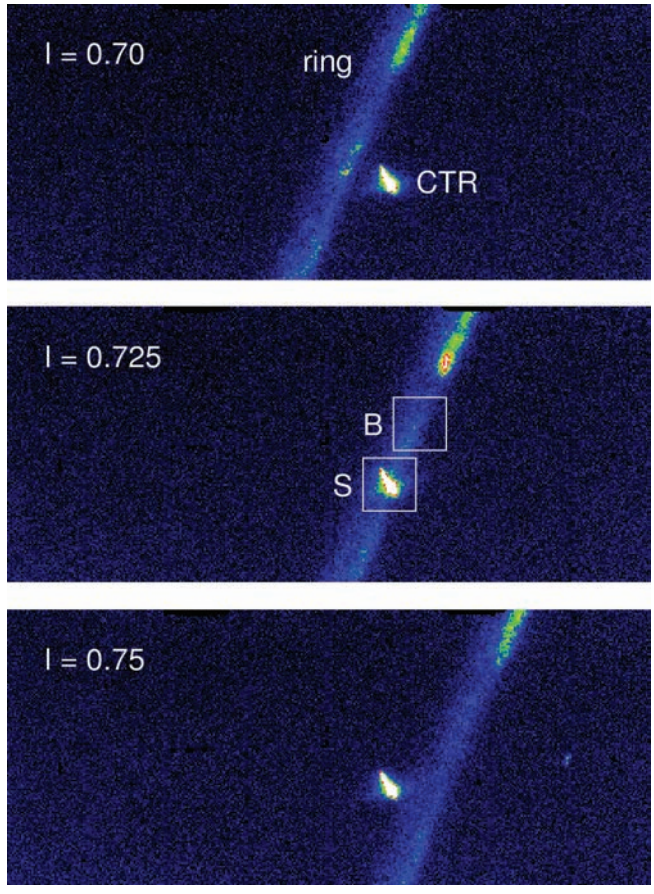

Figure 5
The passage of a Debye–Scherrer ring across a crystal truncation rod (CTR, see text). This artifact originates from the polycrystalline sample holder and, if uncorrected, would result in an anomalously large signal S as extracted from the centre image. This is corrected by choosing an appropriate background signal B placed elsewhere on the ring, as shown. The positions along the CTR in units of the reciprocal-lattice unit perpendicular to the surface l are also given.

inhomogeneities across the sample surface may play a central role. Systematic errors ε are determined by averaging symmetry-equivalent reflections (Robinson, 1991; Bunk, 1999). For each reflection of average intensity I, the standard deviation $\sigma_{\rm std}$ is calculated as the sum of the statistical and systematic errors, *i.e.*

$$\sigma_{\rm std} = [\sigma_{\rm stat}^2 + (\varepsilon I)^2]^{1/2}. \quad (3)$$

Our data have $\sigma_{\rm std} \approx 5\%$, which is on the lower side of the range of values in the literature.

Another advantage of using a pixel detector is that artifacts can be easily recognized and accounted for. For example, Fig. 5 shows the transit of a Debye–Scherrer cone originating from the polycrystalline substrate holder. The data are carefully inspected for such features, which can then be subtracted.

5.2. The incident-beam interception

Many set-ups for experiments with grazing-incidence geometry preclude the possibility of restricting the incident beam so that it does not spill over the front and back edges of the sample surface. For example, if the sample is within a vacuum chamber, it may be quite impractical to position beam-defining slits sufficiently close so that the beam divergence does not extend the beam profile beyond the sample intercept area.

For experiments in which the incident beam spills over the edges of the sample and in which the incident angle varies, such as in reflectivity curves or specular CTRs, it is important to know details of the profile of the beam in the plane containing the incident and specularly reflected beam (here, the horizontal plane), in order to correct the data for the fraction of the incident beam intercepted by the substrate surface.

In many experiments, the incident beam is focused to a certain extent both vertically and horizontally. Hence, measuring the profile by scanning a narrow pair of slits at the detector (either point or pixel) will not accurately record the profile at the sample itself. It is therefore essential to record the profile P by scanning the sample itself across the beam, with the sample surface parallel to the beam axis (*i.e.* $\alpha = 0^\circ$). In the present set-up, this is achieved by scanning the x-translation motor (see Fig. 1). The resulting scan describes the integral of the beam intensity

$$I|_x = \int_{-\infty}^{x} P(x')\,{\rm d}x' \quad (4)$$

as a function of x, an example of which is shown in Fig. 6.

The intensity of the part of the beam intercepted by the sample at an incident angle α is

$$I(\alpha) = \int_{-l}^{+l} P(x)\,{\rm d}x, \quad (5)$$

where $\pm l = (L/2)\sin\alpha$, L being the length of the footprint on the sample surface. $I(\alpha)$ is then directly obtained from the x scan as being simply

$$I(\alpha) = I|_{+l} - I|_{-l}. \quad (6)$$

The raw data are corrected by dividing them by $I(\alpha)$.

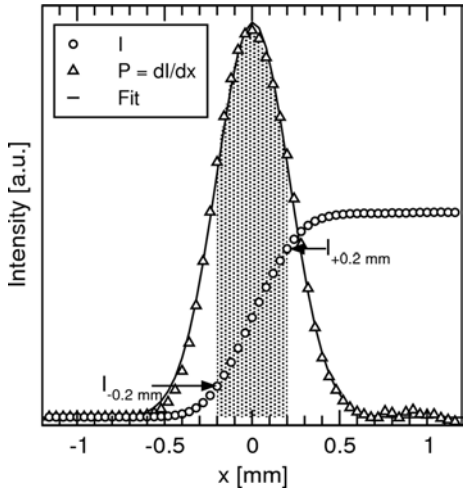

Figure 6
The integrated beam profile can be measured by recording the occlusion of the beam by the sample at $\alpha = 0^\circ$, using the motor x. The fraction of the beam incident on the sample surface (shown here for an incident angle of $2.3^\circ \equiv l = \pm 0.2$ mm) can be directly obtained as the difference of the two values of I at the borders.

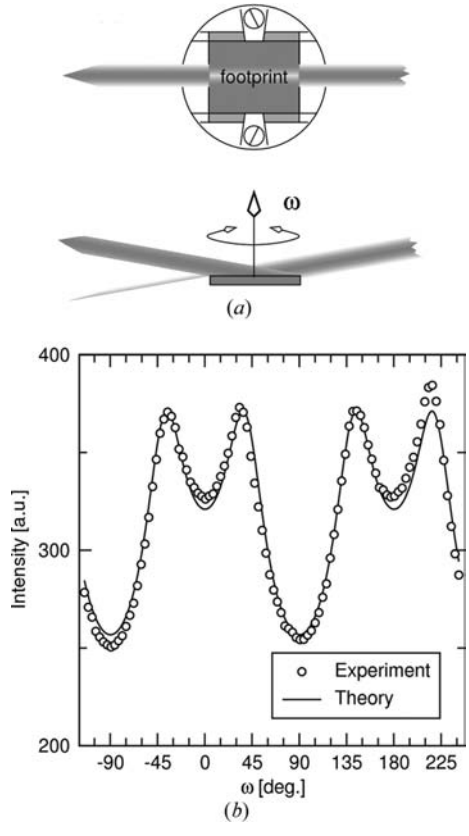

Figure 7
(*a*) The footprint of an overspilling incident beam on non-circular and/or non-concentrically aligned samples changes with rotation angle ω. (*b*) The intensity of an X-ray beam specularly reflected from an 8×10 mm^2 sample surface as a function of ω. This 'camel curve' could be accurately fitted with an analytical function convoluted with an in-plane Gaussian beam profile having a FWHM of 0.94 mm.

5.3. The beam footprint

If the incident beam spills over the edges of the sample surface, rotating the sample around its surface normal will change the footprint unless the sample surface is circular and the rotation axis is exactly coincident with the surface centre. In contrast to experiments that use point detectors and narrow detector slits, which define the fraction of the footprint seen by the detector, the change of the shape and size of the footprint must be corrected for when using an area detector that records the whole diffracted signal. This correction factor therefore takes into account the change in the beam footprint area with rotation angle (here ω). This must be considered, for example, when recording nonspecular CTRs.

This relative change in the footprint size is determined by monitoring the specularly reflected beam intensity $C_f(\omega)$ as a function of rotation of the sample about its surface normal, as shown schematically in Fig. 7(*a*). An example of the obtained curve is given for a rectangular sample surface of 8×10 mm^2 in Fig. 7(*b*). The signal is convolved with the beam profile in the vertical direction, which can be closely approximated as a Gaussian with a full width at half-maximum (FWHM) of 0.94 mm. The theoretical curve, including this convolution, is also shown. The data are corrected for the change in the size of the footprint by dividing by C_f.

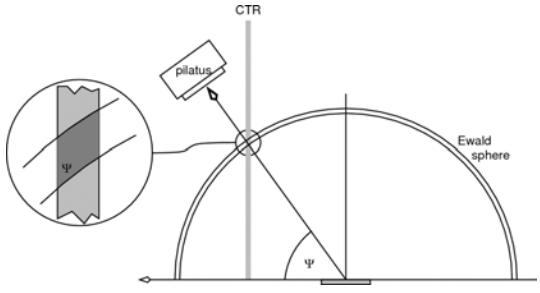

Figure 8
Schematic *k*-space diagram showing the dependence on the portion of the CTR sampled as a function of Ψ.

5.4. Polarization factor

The polarization of the MS beamline is about $p_h = 98\%$ horizontal at 12 keV. The polarization correction factor C_P is

$$C_P = p_h(1 - \cos^2\delta \sin^2\gamma) + (1 - p_h)(1 - \sin^2\delta). \quad (7)$$

5.5. Intercept of the scattered beam with the Ewald sphere

Depending on which source one reads, this correction is either treated separately from the 'Lorentz factor' (see below) or as part of it. Here we describe it separately. As mentioned above, we do not perform a rocking-curve scan when using a pixel detector – in our 'large detector slit stationary mode', the diffractometer simply moves to the calculated angles for the desired (*hkl*), an image is captured and the background subtracted. Consider Fig. 8. It has been previously shown (Specht & Walker, 1993; Vlieg, 1997; Torrelles & Rius, 2004) that the range of *l* involved in the intercept of the CTR with the shell of the Ewald sphere is proportional to $1/\sin\Psi$, where Ψ is the angle subtended by the scattered beam and its projection on the sample plane (see Fig. 1). This means that a larger range of *l* is sampled close to the foot of the CTR than at higher *l*. The integrated signal recorded by the pixel detector must therefore be multiplied by

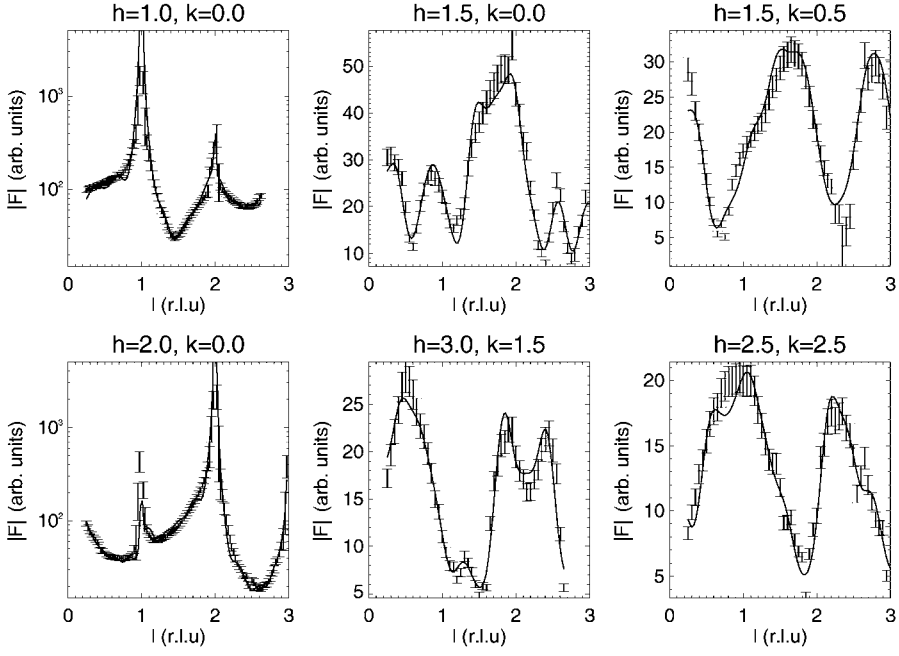

Figure 9
Six representative CTRs and FORs, including fits, taken from a set of 27 CTRs recorded of the surface of $SrTiO_3$(100).

$$C_I = \sin\Psi = \cos\delta\,\sin(\gamma - \alpha), \tag{8}$$

in order to correct for the amount of the vertical component Δl of the CTR that is sampled.

5.6. Lorentz factor

In traditional CTR data acquisition using a point detector, the intensity of the CTR for any given l value is obtained by using a set of slits in front of the detector so that, as the sample is rotated about its normal (ω), the CTR signal will drift pass the slit openings to produce a rocking curve. This is recorded in linear steps in ω, which does not translate to a linear scan in reciprocal space. This must be corrected for before integrating the rocking curve using the Jacobean relationship

$$I(\omega)\,\mathrm{d}\omega = I(k)\,\mathrm{d}k. \tag{9}$$

The situation changes, however, when using a pixel detector in a stationary mode (Specht & Walker, 1993; Torrelles & Rius, 2004). For each l position, no rocking curve needs to be recorded as the detector captures the whole lateral extent of the CTR. Hence, no factor must be considered to correct an integrated rocking curve. Only the factor discussed in the previous subsection needs to be considered.

5.7. Correction summary

The relationship between the recorded data I_R and the corrected data I_C is therefore

$$I_C = I_R \frac{1}{C_f}\frac{1}{C_P}C_I. \tag{10}$$

6. Obtaining an orientation matrix

In the following, it is assumed that the diffractometer and sample have been accurately adjusted and the zeros of the angular movements have been set.

Diffraction experiments involving single-crystal samples in general require a precise knowledge of the orientation of the crystallographic axes in the fixed (normally Cartesian) frame of the diffractometer, in order to navigate reliably in reciprocal space. Software algorithms available to determine this so-called orientation matrix require as an input the precise motor settings (in the example shown in Fig. 1, the values of ω, α, δ and γ) for at least two well defined positions in reciprocal space (normally Bragg peaks) and preferably several more. By using an area detector, this standard procedure is speeded up considerably. This is primarily because (*a*) no detector scans need to be recorded to ascertain the position of the Bragg maximum and (*b*) the large detector area means that it is very probable, using the first estimate for the angle settings, that the CTR will be visible. By tracking this as ω is rotated, the position for the CTR maximum, *i.e.* the Bragg peak, can be very rapidly established.

7. Example

$SrTiO_3$ (STO) is the most commonly used substrate crystal for the thin-film growth of technologically important perovskite materials such as $La_{1-x}Sr_xMnO_3$ and $YBa_2Cu_3O_7$. Despite this, there remains a good deal of ambiguity as to the structure of its surface, which seems to depend strongly on the preparation and processing conditions (Kubo & Nozoye, 2003). In the example given here, an STO substrate was etched using an established method (Koster *et al.*, 1998), resulting in the surface being over 99% TiO_2 terminated and being stable in air. The sample was introduced into an ultra-high-vacuum chamber for the surface diffraction measurements.

In order to obtain a reliable structural model fit to diffraction data, it is necessary that the number of data points $N_{\rm dp}$ considerably exceeds the number of fit parameters $N_{\rm fp}$. Fig. 9 shows a representative selection of six CTRs and their fits from a data set of 27 CTRs (containing over 1800 data points)[2] of the surface of (100)-oriented STO (Herger *et al.*, 2005). The time required to record this data set was about 10 h. It has been fitted to a model of a surface region (*i.e.* one that differs structurally from that of the bulk) down to four unit cells and a mixture of surface terminations, involving approximately $N_{\rm fp} = 200$ fitting parameters. As far as the authors know, this represents the most complex system yet investigated using surface diffraction. This large data set could only be brought to bear on this problem in the limited synchrotron beamtime available, thanks to the accelerated acquisition rate offered by the pixel detector. The full data set and the model will be described in detail elsewhere (Herger *et al.*, 2005).

8. Future developments and conclusions

A new pixel detector module is presently being commissioned, having an array size of 487×195 pixels and a pixel size of 172 µm. The number of dead and unreliable pixels has been reduced to essentially zero. The maximum count rate is 1 MHz and the maximum number of counts per pixel is 10^6. The detector is to be protected from overexposure to X-rays by a large-aperture ionization chamber (IC) at the entrance to the collimating tube in front of the detector. Overexposure will trigger a fast photon shutter upstream of the diffractometer within 0.1 s and a slow shutter between the IC and the pixel detector. Once the slow shutter is closed, the fast shutter can be reopened and the transmission reduced using filters until the signal from the IC drops below a predefined level.

In conclusion, the use of a pixel detector instead of a point detector in grazing-incidence and surface diffraction experiments has greatly improved reliability and increased the data acquisition rate by approximately an order of magnitude. This opens up new possibilities of investigating more complex

[2] The step size in l was chosen in advance to be small enough to capture all but the most rapidly changing features, *i.e.* 0.025 for the CTRs and 0.05 for the FORs). In the case of the FORs, it can be seen from Fig. 9 that this estimate was clearly justified, although for the CTRs a reduction by a factor of 2 could have been tolerated.

crystalline systems within the restricted time available for synchrotron users and the limited lifetime of maintaining a clean and well defined sample surface.

The authors gratefully acknowledge F. Glaus, M. Naef and H. Rickert for their assistance in the production of the pixel detector.

References

Als-Nielsen, J. & McMorrow, D. (2001). *Elements of X-Ray Physics.* New York: John Wiley and Sons.

Alvarez, J., Lundgren, E., Torrelles, X. & Ferrer, S. (2000). *Surf. Sci.* **464**, 165–175.

Brönnimann, Ch., Eikenberry, E. F., Horisberger, R., Hülsen, G., Schmitt, B., Schulze-Briese, C. & Tomizaki, T. (2003). *Nucl. Instrum. Methods Phys. Res. A*, **510**, 24–28.

Bunk, O. (1999). PhD thesis, Department of Physics, University of Hamburg, Germany. http://www.sub.uni-hamburg.de/opus/volltexte/1999/99/.

Eikenberry, E. F., Brönnimann, Ch., Hülsen, G., Toyokawa, H., Horisberger, R., Schmitt, B., Schulze-Briese, C. & Tomizaki, T. (2003). *Nucl. Instrum. Methods Phys. Res. A*, **501**, 260–266.

Feidenhans'l, R. (1989). *Surf. Sci. Rep.* **10**, 105–188.

Herger, R., Willmott, P. R., Schlepütz, C. M., Bunk, O. & Patterson, B. D. (2005). In preparation.

Jensen, M. V. R. S., Dye, D., Janes, K. E., Korsunsky, A. M., Roberts, S. M. & Reed, R. C. (2002). *Metall. Mater. Trans. A*, **33**, 2921–2931.

Koster, G., Kropman, B., Rijnders, G., Blank, D. & Rogalla, H. (1998). *Appl. Phys. Lett.* **73**, 2920–2922.

Kubo, T. & Nozoye, H. (2003). *Surf. Sci.* **542**, 177–191.

Patterson, B. D., Abela, R., Auderset, H., Chen, Q., Fauth, F., Gozzo, F., Ingold, G., Kühne, H., Lange, M., Maden, D., Meister, D., Pattison, P., Schmidt, T., Schmitt, B., Schulze-Briese, C. *et al.* (2005). *Nucl. Instrum. Methods Phys. Rev. A*, **540**, 42–67.

Robinson, I. K. (1991). *Handbook on Synchrotron Radiation*, edited by G. S. Brown & D. E. Moncton, Vol. 3, ch. 7, pp. 221–226. Amsterdam: North Holland.

Robinson, I. K. & Tweet, D. J. (1992). *Rep. Prog. Phys.* **55**, 599–651.

Specht, E. D. & Walker, F. J. (1993). *J. Appl. Cryst.* **26**, 166–171.

Tancret, N., Roussel, P. & Abraham, F. (2004). *J. Solid State Chem.* **177**, 806–816.

Torrelles, X. & Rius, J. (2004). *J. Appl. Cryst.* **37**, 395–398.

Vlieg, E. (1997). *J. Appl. Cryst.* **30**, 532–543.

Vlieg, E. (1998). *J. Appl. Cryst.* **31**, 198–203.

You, H. (1999). *J. Appl. Cryst.* **32**, 614–623.